

Article

Co(II/III) Complexes with Benzoxazole and Benzothiazole Ligands as Efficient Heterogenous Photocatalysts for Organic Dyes Degradation

Martyna Szymańska ¹, Włodzimierz Czepa ^{1,2}, Cezary Hołubowicz ³, Renata Świsłocka ⁴,
Teresa Łuczak ¹, Maciej Kubicki ¹, Joanna Karpińska ³, Marta A. Fik-Jaskółka ^{1,*} and
Violetta Patroniak ^{1,*}

¹ Faculty of Chemistry, Adam Mickiewicz University, Uniwersytetu Poznańskiego 8, 61-614 Poznań, Poland; martyna.szymanska@amu.edu.pl (M.S.); wlodekczepa@gmail.com (W.C.); telucz@amu.edu.pl (T.Ł.); mkubicki@amu.edu.pl (M.K.)

² Centre for Advanced Technologies, Adam Mickiewicz University, Uniwersytetu Poznańskiego 10, 61-614 Poznań, Poland

³ Faculty of Chemistry, University of Białystok, Ciołkowskiego 1K, 15-245 Białystok, Poland; czarekk96@gmail.com (C.H.); joasia@uwb.edu.pl (J.K.)

⁴ Faculty of Construction and Environmental Engineering, Białystok University of Technology, Wiejska 45e, 15-351 Białystok, Poland; r.swislocka@pb.edu.pl

* Correspondence: martafik@amu.edu.pl (M.A.F.-J.); violapat@amu.edu.pl (V.P.)

Received: 8 October 2019; Accepted: 30 October 2019; Published: 1 November 2019



Abstract: The problem of pollution in the current world is growing, however people's awareness of environmental protection and ecology is also increasing. The aim of the study is to present three new Schiff base compounds with Co(II/III) ions and to assess their photocatalytic activity. The study was supported by cyclic voltammetry technique. In due course the complex **2** revealed as the most effective in AR18 degradation, even more than commercially available TiO₂. The search for new photocatalysts able to decompose harmful organic dyes into environmentally friendly basic substances is becoming a new trend in the area of chemistry development.

Keywords: Schiff base; cobalt(II/III) complexes; photocatalysis; cyclic voltammetry; redox processes

1. Introduction

Nowadays the natural environment is becoming more and more exposed to the threat of pollution. In the past decades the growing food, textile, chemical etc., industries have led to the alarming level of the Earths' contamination. Currently, the trend is to maintain the high efficiency of the factories and to decrease the amount of post-production and post-usage waste. Both, the big industries and consumers joined the pro-Earth movement and support the low-waste lifestyle to prevent further contaminations [1]. However, since the level of pollution is already very high, it is important to develop new and efficient ways to decrease it. Notably, over 100,000 organic dyes is used worldwide in the manufactures [2,3]. One of the challenges is the removal of the organic dyes, used in textile, paper, polymer, cosmetics, and food industry from wastewater [4]. Organic dyes, such as Reactive Blue 21 and Acid Red 18 and the products of their cleavage exhibit carcinogenic and mutagenic effects when present in high concentrations [5–7]. In fact, the list and usage protocols of textile dyes that decompose to toxic amines are not regulated yet [8]. Therefore, there is a strong need to find a way to efficiently reduce the amount of dyes already present in the environment.

The significance of adsorption of noxious compounds is dropping, since it does not neutralize dyes to non-toxic compounds, but only removes it from water [9]. The challenge is to decompose

the compounds to its harmless derivatives that can be achieved by catalytic degradation. The perfect catalysts exhibiting efficient decomposition of organic dyes should be cheap, as well as easy to obtain and to operate [10]. In particular, photocatalysis is a modern green chemistry approach which breaks down organic pollutants into simple, non-toxic compounds such as water, carbon dioxide, and other simple inorganic anions under the influence of photocatalyst and UV irradiation or even visible light. It is already shown that photocatalysis is a useful and promising tool for efficient degradation dyes from wastewater [11,12].

One of the most commonly used photocatalyst is titanium dioxide (TiO_2)—a cheap, non-toxic, and stable compound. Notably, TiO_2 needs to be exposed to UV light to catalyze the degradation processes. UV accounts only for *ca.* 2% of the sunlight, while visible light is *ca.* 45%. Therefore, a new class of catalysts with high photocatalytic activity in the presence of visible light is needed and recently widely explored [13,14]. Doping of the TiO_2 with Schiff base complexes increases the photocatalytic activity because of the action in the wider range of sunlight—both UV and visible light. The degradation of methylene blue in the visible light using the modified hybrid compounds was examined by M. M. Momeni [15].

Since the d-electron metal ions may adsorb visible light, some of the complexes exhibit enhanced photocatalytic performance toward organic compound degradation. Therefore, there is a number of papers presenting outstanding efficiency of the process in the presence of complexes with such metal ions as Zn(II), Co(II), Ni(II), Cu(II), Fe(II) [16–19].

One of the degradation pathways bases on the oxidation mechanism called *Fenton reaction*—a well-known reaction utilizing H_2O_2 and iron ions. The homogenous catalyst under electromagnetic radiation produces hydroxyl radicals providing effective decomposition of organic species [20]. This reaction is widely used for destroying hazardous organics including aromatic amines, surfactants, and organic dyes [21–23]. Therefore, such an approach inspires the development of a class of new efficient compounds with photocatalytic activity. An example could be the mechanism of the methylene blue decolorization process in the presence of Co^{2+} , HCO_3^- , and H_2O_2 forming the Fenton-like Co^{2+} - HCO_3^- - H_2O_2 system that was presented by Li et al. [24,25]. Thanks to this, organic impurities could be oxidized easily. Moreover, in another case peroxide decomposition was catalyzed by Co^{2+} ions [26].

As the degradation of organic dyes is promoted by electron transfer, to better understand photocatalytic behavior of cobalt complexes, cyclic voltammetry (CV) was performed. CV is a valuable technique for investigation of a variety of redox processes. Moreover, it might provide a wide range of characterization showing its potential in photocatalytic reactions including stability of the compounds, presence of intermediates during redox reactions, and reversibility of the processes [27].

Because of the previous research in our group [28], we decided to check the photocatalytic activity of complexes 1–3 based on Co(II/III) metal ions with the following model textile and food dyes: Reactive Blue 21 (RB21) and Acid Red 18 (AR18) (Figure 1). Also electrochemical measurements for all complexes and ligands were investigated.

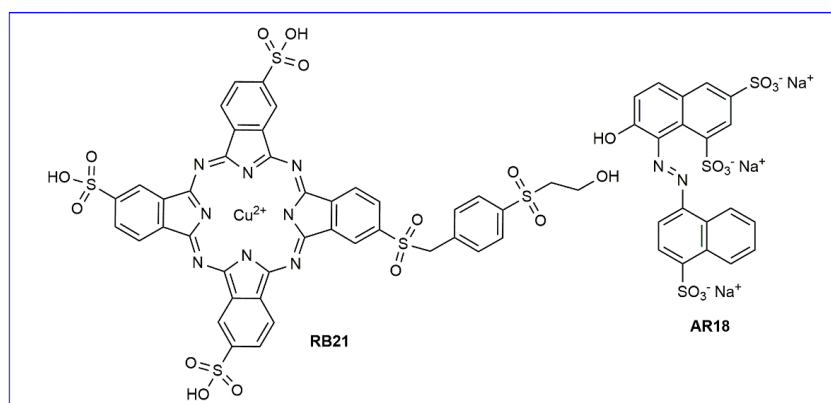


Figure 1. Molecular structures of dyes used in presented studies: Reactive Blue 21 (RB21) and Acid Red 18 (AR18).

2. Results and Discussion

2.1. Synthesis and Characterization

Three Schiff base type ligands **HL**¹, **L**², and **L**³ comprising three-donor-binding-units (Figure 2) were synthesized in a two-step protocol via (i) nucleophilic substitution of 2-chlorobenzothiazole (**HL**¹ and **L**²) or 2-chlorobenzoxazole (**L**³) with excess of 1-methylhydrazine and (ii) condensation of thus obtained products with salicylaldehyde (**HL**¹) [29] or 2-pyridinecarboxaldehyde (**L**² and **L**³) [28,30]. The selected ligands exhibit different coordination motifs (NNO in **HL**¹ vs. NNN in **L**²/**L**³). Synthesized ligands were obtained as light yellow solids in 78.0–86.4% yields. Their purity was confirmed by ¹H NMR, ¹³C NMR, ESI-MS, IR, and elemental analysis. Thus the obtained ligands were reacted with Co(ClO₄)₂ (**HL**¹) and with Co(NO₃)₂ (**L**² and **L**³) in a 1:1 ligand:salt molar ratio. The salts choice was driven by the ability of complexes to crystallize and their water insolubility—an essential feature of heterogeneous catalysts. Since perchlorates are non-coordinating anions complex **1** has a closed coordination sphere fulfilled with two molecules of ligand **HL**¹. On the contrary, nitrates are good coordinating agents, hence complexes **2** and **3** are coordinated by one molecule of ligand and nitrates (complex **2**) or nitrates and methanol (in case of complex **3**). All complexation reactions were carried out in methanol for 24 hours at room temperature and isolated with yields of 59–67% by precipitation with diethyl ether from concentrated solutions. Monocrystals suitable for X-ray measurements were obtained by a slow diffusion of diethyl ether (complex **1**) or diisopropyl ether (complexes **2** and **3**) into the methanolic solutions of appropriate complexes.



Figure 2. Structures of ligands **L**¹–**L**³ and schematic representation of complexes they form with Co(II/III) ions.

Complex **1** has an octahedral coordination sphere filled by two deprotonated NNO-donor ligands **L**¹. Complexes **2** and **3** are coordinated by only one ligand molecule (**L**² and **L**³, respectively) and the remaining coordination sites are occupied by nitrates and/or methanol. In complex **1** the Co(II) has oxidized to Co(III) in the reaction course. It occurs most probably because of the presence of OH groups in the ligand.

2.2. Description of the Structures

In all cases the ligand molecules act as three-dentate ligands, with N3, N12, and either pyridine nitrogen (**2**, **3**) or hydroxyl oxygen (**1**) atoms as coordination centers (cf. Table S1).

Interestingly, all three ligands make three different complex structures. Ligand **L**¹ crystallizes as the cationic species of [Co(**L**¹)₂](ClO₄) composition with perchlorates as counteranions; the coordination of the Co center is quite regular octahedron (cf. Suppl. Mat., Figure S1, Table S1).

The neutral complex **2** has the composition [Co**L**²(NO₃)₂] and the coordination number is 7 (Figure 3). Besides three ligand donor atoms two oxygen atoms from each nitro group are coordinated

to metal center. The distances Co-N and Co-O are almost equal, in the range 2.16–2.25 Å (cf. Table S2). The coordination polyhedron can be best described as distorted one-capped octahedron.

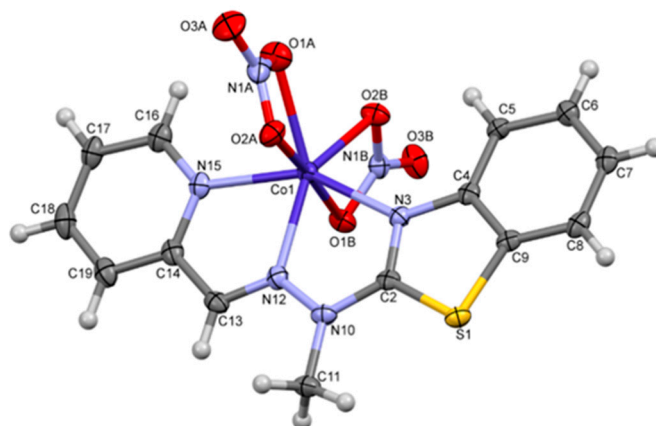


Figure 3. Perspective view of the complex **2**; ellipsoids are drawn at the 50% probability level hydrogen atoms are represented by spheres of arbitrary radii.

In turn complex **3** besides ligand molecule and two nitro groups has also a methanol molecule in the coordination sphere (Figure 4). Coordination number is 6 (octahedral geometry) as each nitro group is coordinated with only one oxygen atom. Table S2 shows that the Co-O bonds are significantly shorter than in case of **2**; the shortest non-bonding intramolecular Co . . . O contacts are in this case as long as 3.14 Å.

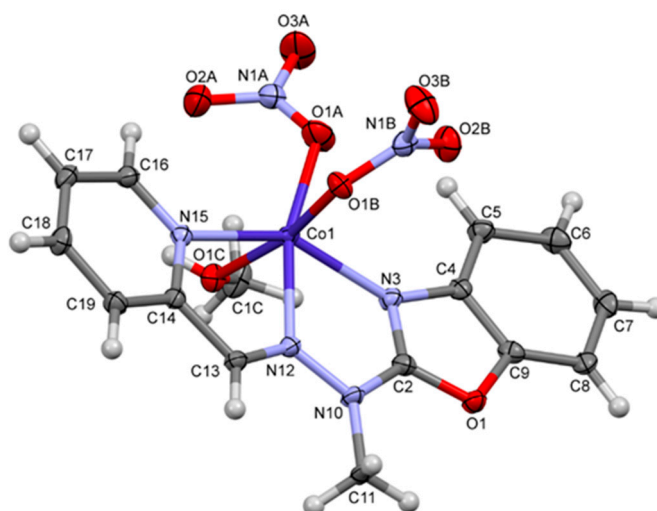


Figure 4. Perspective view of the complex **3**; ellipsoids are drawn at the 50% probability level; hydrogen atoms are represented by spheres of arbitrary radii.

2.3. Cyclic Voltammetry

In order to gain some insights into the redox-richness of studied systems their electrochemical properties were studied by cyclic voltammetry (CV). The experiments were performed in deaerated DMF supplemented with 0.1 M TBAP as the supporting electrolyte solution (SES). The cycles were scanned continuously starting from the cathodic potential limit, going to positive direction, up to the anodic potential limit and then going back to negative direction up to the cathodic potential limit at least three times (until stabilization of the CV signals). Figure S2 represents electrochemical behavior of the polycrystalline gold electrode in the presence of SES (peaks at $E_1 = 1.64$ V vs. SCE and $E_2 = 0.75$ V vs. SCE correspond to the formation of the gold oxide layer at the electrode surface and its

reduction, respectively [31,32]). As it was established earlier, a peak visible at the anodic branch of CV at about -0.75 V vs. SCE arising from a negative to positive potential limit must be associated with electroactivity of the tetrabutylammonium cation (TBA^+) [33], whereas two peaks which appeared in the CV of SES at -0.52 and -1.05 V vs. SCE going from a positive to negative potential limit at the cathodic branch of considered CV are assigned to the redox processes related to DMF molecules. It was observed that the latter effect is intensified when ligands or, especially, complexes are added into the supporting electrolyte solution [33]. The cyclic voltammograms of SES recorded in the presence of ligands HL^1 - L^3 and their Co(II/III) complexes 1-3 are presented in Figures 5 and 6, respectively. It should be emphasized that in the case of all tested ligands and their complexes the current values at a given electrode potential were already stable in the third cycle. The fourth and subsequent CVs overlap with the third ones. For this reason the curves obtained in third cycles are shown herein. The CV investigation of all of the studied complexes showed that the higher concentration of compounds the more feasible the oxidation processes are and it is compatible with the Randles-Sevcik equation (Figures S3-S5) [34].

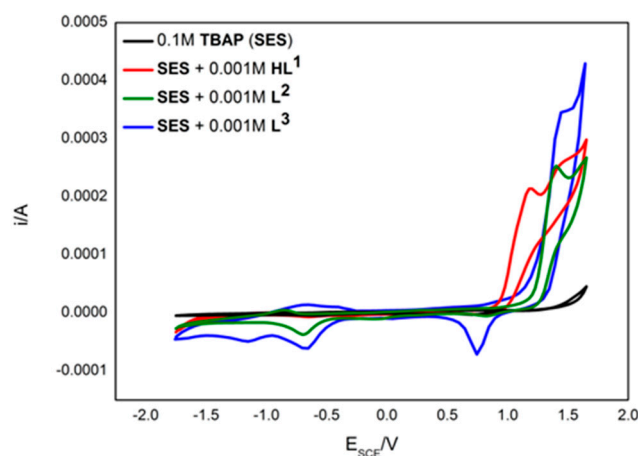


Figure 5. Cyclic voltammograms of the polycrystalline gold electrode in basic electrolyte 0.1 M TBAP in DMF and ligands HL^1 - L^3 .

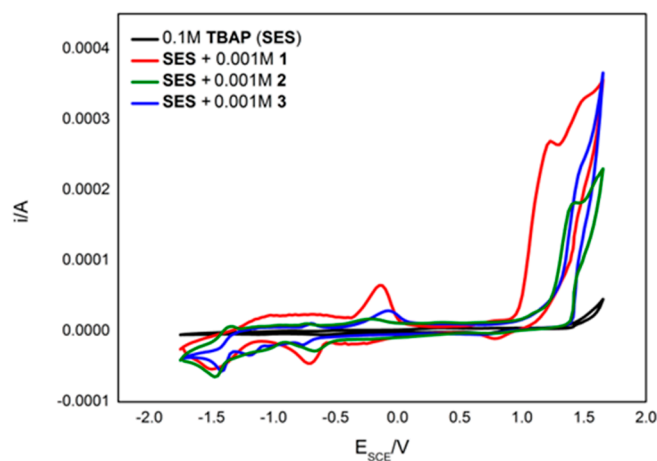


Figure 6. Cyclic voltammograms of the polycrystalline gold electrode in basic electrolyte 0.1 M TBAP in DMF and complexes 1-3.

All three ligands oxidize in the potential range of the gold oxide layer formation (Figure 5). In case of HL^1 and L^2 the oxidation is irreversible. It is well known that sulfur has a high affinity toward gold [35], so taking this into account these two ligands may attach to the electrode surface with their

benzothiazole moieties [36]. Thus, the latter may be responsible for the irreversible nature of **HL**¹ and **L**² oxidation.

One can see that ligand **HL**¹ is easily oxidized. Its oxidation starts at lower electrode potential relative to the ligand **L**². This observation may prove that the presence of OH groups in the **HL**¹ ligand structure has an effect on the feasibility of oxidation process.

On the other hand, the oxidation of **L**³ has a quasi-reversible nature [34]. In this case in the cyclic voltammogram the oxidation peak appears at $E = 1.45$ V vs. SCE and the reduction peak at $E = 0.75$ V vs. SCE is visible, respectively (Figure 5). Although the difference in the potential of oxidation and reduction peaks is characteristic of a reversible electrode process, the ratio of the current value in the oxidation peak to the value of the current in the reduction peak of **L**³ is significantly less than 1, which makes the considered process quasi-reversible. In case of this ligand the high anodic current values observed during oxidation are most likely due to the formation of the radical cation of the benzoxazole part of the ligand [37]—in our previous work it was established that this process is not related to reduction of pyridine moiety [33]. One may envisage that the quasi-reversibility of the redox processes is possible since the benzoxazole moiety does not adsorb on gold surface.

Figure 6 shows the redox behavior of complexes 1–3. “Closed” complex 1—the only one among the investigated complexes with coordination sphere occupied by two organic ligands (**L**¹)—exhibits a quasi-reversible redox process with pair of peaks at $E_1 = -0.14$ V and $E_2 = -0.70$ V vs. SCE which is attributed to the Co(II)↔Co(III) redox process (Figure S6 shows comparison of cyclic voltammograms of **HL**¹ and 1). For the complexes 2 and 3 the process of irreversible oxidation is observed as evidenced by the oxidation peaks at potentials $E = -0.22$ V and $E = -0.07$ V for 2 and 3, respectively (the comparison of cyclic voltammograms of **L**² together with 2 and **L**³ with 3 show Figures S7 and S8, respectively). One may conclude that the presence of labile coordination sites of the Co(II) ions promote the irreversible oxidation of metallic centers in studied complexes (Figure 6).

2.4. Photostability and Photodegradation Studies

First, the photostability of complexes 1–3 in the solid state was confirmed. For this purpose the FT-IR and PXRD spectra of complexes were recorded. Then the complexes were irradiated for 120 min with UV radiation ($\lambda = 256$ nm) or in the imaging chamber of a solar light simulator emitting light in the 300–800 nm range. It was followed by the re-recording of the FT-IR and PXRD spectra (Figures S10–S15) which showed no significant perturbation of the complexes structure. Therefore, it could be stated that complexes are photoresistant.

Reactive Blue 21 (RB21) and Acid Red 18 (AR18) were used as the model dye contaminants for the examination of the photocatalytic activities of the presented complexes with Co(II/III) ions. The UV-Vis spectra of dyes are presented in Figures S16 and S17. RB21 possess 4 maxima at 210, 334, 624, and 664 nm. The second dye AR18 has 4 peaks at 214, 246, 334, and 508 nm. The analytical wavelengths chosen for the monitoring of the decomposition processes of the RB21 and AR18 are 664 nm and 508 nm, respectively.

First, the self-decomposition of dyes under irradiation was monitored by measuring the absorbance at their analytical wavelengths. The obtained data showed that the slow bleaching occurred in the solutions of both dyes. The values of observed rates pointed that Reactive Blue 21 is more stable than Acid Red 18 and in this case this effect may be omitted (Table 1). The observed differences in the stability of both compounds can be attributed to their molecular structure. Reactive Blue 21 belongs to the phthalocyanine group of dyes which are characterized by resistance to the light (especially Cu phthalocyanines complexes) [38] while Acid Red 18 is a representative of azo-dyes group which is more labile to excitation by UV-Vis irradiation [39]. In the following step, the influence of complexes 1–3 on the photolysis of dyes was investigated and TiO₂ was used as a control photocatalyst. Reported processes were assumed to follow first-order kinetics. The obtained data are summarized in Table 1.

Table 1. Kinetic characteristic of the studied processes.

Entry	Dye	Source of Irradiation	Type of Photolysis	Kinetic Constant k [min^{-1}]
1	Reactive Blue 21	Sunlight	self-decomposition	7×10^{-4}
2		254 nm		8×10^{-4}
3		Sunlight	TiO ₂ -catalyzed	4.9×10^{-3}
4		254 nm		4.1×10^{-3}
5		Sunlight	1-catalyzed	7×10^{-4}
6		254 nm		2.5×10^{-3}
7		Sunlight	2-catalyzed	2.6×10^{-3}
8		254 nm		1.2×10^{-3}
9		Sunlight	3-catalyzed	5×10^{-4}
10		254 nm		na *
11	Acid Red 18	Sunlight	self-decomposition	1.5×10^{-3}
12		254 nm		0.4×10^{-3}
13		Sunlight	TiO ₂ -catalyzed	1.6×10^{-3}
14		254 nm		0.3×10^{-3}
15		Sunlight	1-catalyzed	6×10^{-4}
16		254 nm		na *
17		Sunlight	2-catalyzed	2.3×10^{-3}
18		254 nm		2.5×10^{-3}
19		Sunlight	3-catalyzed	0–45 min induction period 45–120 min $K = 8 \times 10^{-4}$
20		254 nm		na *

k = kinetic rate constant of the first order reaction; * na = not active.

Complex **2** appeared to be the most efficient catalyst in the degradation of organic matter when compared to the other two complexes. The effect is especially visible in the case of AR18 degradation. In this case complex **2** accelerates the decomposition of the dye almost twice more efficiently than the control catalyst TiO₂ in the sunlight and eight times more under UV irradiation. Interestingly, complexes **1** and **3** are not active when irradiated only with UV irradiation.

Complex **1** has a “closed” coordination sphere filled with two organic ligands **HL**¹ which makes it less active as a photocatalyst in comparison to the complexes **2** and **3**. The lack of labile coordination sites impedes the photocatalytic action because of the hindrance of active center of photocatalyst which is the metal ion [28]. This can also be affected by the quasi-reversible redox processes related to the metallic center of complex **1**. Furthermore, between the “open” complexes, the complex **2** is more active than complex **3** in degradation of AR18. In both complexes the oxidation of metallic center is non-reversible; therefore one needs to look for the source of differences in the coordinated ligands. Ligand **L**³ comprising benzoxazole moiety is quasi-reversibly oxidized [40], while ligand **L**² with benzothiazole moiety is not susceptible to reversible electrochemical processes [41]. It leads to a conclusion that the more electrochemically stable compound, the better photocatalyst it is [42]. Additionally, in the case of photodegradation of AR18 catalyzed by complex **3**, the induction period was observed during which the color reduction was unnoticeable. After 45 min a slight discoloration of the solution occurred. Probably, this phenomenon is caused by too low concentration of reactive oxygen species (ROS) on the surface of the catalyst.

In general the observed low photocatalytic efficiency of the used catalysts may be a result of the strong absorption of the light by dyes and the competition for light between catalysts and studied dyes [43].

Proposed mechanism of dyes solution bleaching degradation is presented in Figure 7. As a result of light absorption the electrons move from the valence band to the conductivity band which generates the holes (h^+) in HOMO level. It is followed by the reduction of the oxygen molecules and subsequent water oxidation. Thus formed reactive oxygen species (ROS) recombine with the organic dyes and induce their decomposition to photoproducts—less complex molecules [44]. In the case of Reactive Blue 21 the cleavage of nitrogen bonds in the inner ring of the phtalocyanine molecule and release of Cu^{2+} ion is suggested [45] as the first step of degradation. The bleaching of Acid Red 18 solution is most likely the result of the reaction of a hydroxyl radical with an azo group, cleaving it in two substituted naphthalene molecules [46].

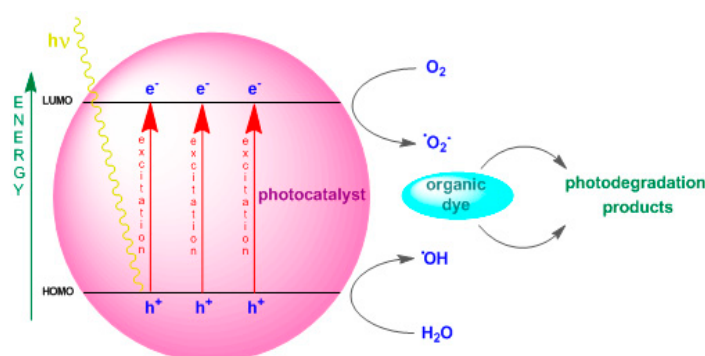


Figure 7. Mechanism of dye degradation by complex compounds.

The presented results are very primary. The goal of the performed experiments was to check if the newly synthesized Co-benzothiazole and benzoxazole complexes exhibit photocatalytic activity. The obtained results seem to be promising and show some photocatalytic activity of the studied Co complexes.

2.5. Optical Properties of Compounds

In order to determine and better understand the photocatalytic efficiency, the HOMO-LUMO energy gaps in the ligands HL^1-L^3 and the complexes 1–3 were calculated. First, the reflectance spectra (ATR) have been recorded in the range from 400 to 4000 nm, however, the HOMO-LUMO energy gaps have been calculated for the visible range of 800–400 nm. Then, the diffuse reflectance spectra were transformed using the Kubelka–Munk function and a dependency $[(F(R)hv)^2/(eVcm^{-1})^2]$ versus $hv/(eV)$ was obtained, where: $F(R)$ is the Kubelka–Munk function [$F(R) = K/S$], K is molar reflectance coefficient [$K = (1-R)^2$], and S is the scattering factor [$S = 2R$]. Radiation energy was calculated from the formula: $1240/\lambda$. The values of the optical energy gaps of the tested compounds are presented in Table 2.

Table 2. Calculated energy gaps for all compounds.

	HL ¹	L ²	L ³	1	2	3
Energy gap [eV]	1.550	2.205	1.625	1.774	1.774	1.621

The key task is to create photocatalytically active compounds with a smaller energy gap than the one of TiO_2 which is 3.2 eV. Lowering the HOMO-LUMO gap enables using the visible light for catalytic reactions which accounts for almost 50% of the sunlight [47]. In general, a good photocatalyst has a large enough energy gap ($E_g > 1.23$ eV) to provide energetic electrons and at the same time small enough to overlap with the solar spectrum [42,48].

All of the described complexes herein fulfill this requirement, since their energy gaps are *ca.* 1.62–1.77 eV. By using Co(II) ions instead of Ag(I) we were able to lower the energy gap from the level of *ca.* 2.7 eV [28] and potentially utilize the visible light more efficiently. It stays in a good agreement with the photocatalytic measurements which showed that complex **1** and **3** are not active when irradiated with the UV light. Complex **2**, the only one which is electrochemically inert is at the same time a more efficient catalyst of AR18 degradation than TiO₂ when irradiated in the solar simulator.

3. Materials and Methods

3.1. Materials and Physical Measurements

The organic substrates and metal salts were used without further purification as supplied from Sigma Aldrich (Darmstadt, Germany). Microanalyses were performed using a Perkin Elmer 2400 CHN microanalyzer. ESI-MS spectra for CH₃CN solutions at concentration $\sim 10^{-4}$ M were measured using a Waters Micromass ZQ spectrometer. (Micromass&Waters; Milford, USA) The electronic-absorption titration spectra were recorded with a Hitachi U-2800A spectrophotometer (Hitachi, Tokyo, Japan) at a scan speed of 1200 nm \times min⁻¹ and a spectral bandwidth of 1.5 nm. The photocatalytic degradation and photolysis experiments were performed with a solar simulator (SUNTEST CPS+, Atlas, Mount Prospect, IL, USA) equipped with a xenon lamp that emits radiation similar to sunlight ($\lambda = 300\text{--}800$ nm). The intensity of the source radiation (E_s), generally defined as the fraction of the absorbed light power per unit of the surface area was 500 W \times m⁻² which corresponds to the intensity of irradiation of the value 2.32×10^{-6} einstein \times m⁻². In the photostability studies the FT-IR spectra were recorded in the range between 400 and 4000 cm⁻¹ using a Nicolet 6700 FTIR Spectrometer Thermo Scientific (Thermo Scientific, Waltham, MA, USA), equipped with a single-reflection diamond ATR accessory with a spectral resolution 4 cm⁻¹. The ATR spectra were recorded in the range between 399.19 and 4001.57 cm⁻¹ using a Nicolet 6700 or Thermo Scientific Nicolet Magna 500 equipped with a single-reflection diamond ATR accessory (32 scans with resolution 2 nm). Spectrophotometer UV-Vis-NIR Jasco equipped with an integrating sphere was used for recording the diffuse-reflectance (DR) spectra of the studied compounds. DR spectra were recorded in the range from 399.19 to 4001.57 nm with the speed scan 400 nm \times min⁻¹. The PXRD patterns were recorded with an X-ray diffractometer Agilent Technologies SuperNova equipped with molybdenum hollow cathode lamp (Santa Clara, CA, USA). Electrochemical measurements were performed using the Autolab potentiostat/galvanostat analyzer (AUTOLAB PGSTAT 302N, Eco Chemie, B. V., Utrecht, The Netherlands) and a three-compartment cell separated by glass frits. For water purification the TKA MicroPure-system (Niederelbert, Germany) was used.

3.2. Synthesis of Ligands

Ligands **HL**¹-**L**³ (Figure 2) were prepared according to the synthetic procedures reported previously, **HL**¹ [29], **L**² [28], and **L**³ [30].

3.3. Synthesis of Complexes (1–3)

3.3.1. Complex 1 [Co^{III}(L¹)₂]

Ligand **HL**¹ (24.0 mg, 84.7 μ M) was dissolved in 5 mL MeOH. After addition of Co(ClO₄)₂·6H₂O (31.0 mg, 84.7 μ M) the mixture changed color from yellow into orange. Reaction was carried out for 24 hours at room temperature. Complex was isolated as an orange powder by evaporation of the solvent to *ca.* 1 mL and precipitation with excess of Et₂O. Monocrystals suitable for X-ray analysis were obtained by slow diffusion of Et₂O into a solution of the complex **1** in MeOH at 4 °C. Yield: 59% (14.16 mg)*.

ESI-MS(+) m/z (%): 284 (100) [**L**¹+H]⁺, 624 (35) [Co(**HL**¹)**L**¹]⁺; ESI-MS(-) m/z (%): 282 (100) [**L**¹-H]⁻. Anal. calcd. for C₃₀H₂₆N₆O₂S₂Co (625.63): C, 57.6; H, 4.2; N, 13.4%; found: C, 56.9; H, 4.0;

N, 12.8%. IR (ATR, cm^{-1}): $\nu(\text{O-H})_s$ 3434; $\nu(\text{C-H})_{\text{imin}}$ 3063; $\nu(\text{C=C})_{\text{ar}}$ 1601, 1573, 1531; $\nu(\text{C=N})$ 1531; $\nu(\text{C-N})$ 1292; $\nu(\text{C-O})$ 1096; $\gamma(\text{C-H})_{\text{ar}}$ 972, 918, 879, 751; $\nu(\text{C-S})$ 640.

3.3.2. Complex 2 $[\text{Co}^{\text{II}}\text{L}^2](\text{O}_2\text{-NO})_2$

Ligand L^2 (9.13 mg, 34.0 μM) was dissolved in 5 mL MeOH. After addition of $\text{Co}(\text{NO}_3)_2 \cdot 6\text{H}_2\text{O}$ (9.37 mg, 34.0 μM) the mixture changed color from yellow to orange. Reaction was carried out for 24 hours at room temperature. Complex was isolated as an orange powder by evaporation of the solvent to ca. 1 mL and precipitation with excess of Et_2O . Brownish monocrystals suitable for X-ray analysis were obtained by slow diffusion of *i*-Pr₂O into the solution of the complex 2 in MeOH at 4 °C. Yield: 66.8 % (10.97 mg)*.

ESI-MS(+) *m/z* (%): 163 (15) $[\text{CoL}^2]^{2+}$, 389 (100) $[\text{CoL}^2(\text{NO}_3)]^+$; ESI-MS(-) *m/z* (%): 245 (30) $[\text{Co}(\text{NO}_3)_3]^-$. Anal. calcd. for $\text{C}_{14}\text{H}_{12}\text{N}_6\text{O}_6\text{SCo}$ (451.28): C, 37.26; H, 2.68; N, 18.62%; found: C, 35.39; H, 2.82; N, 17.75%. IR (ATR, cm^{-1}): $\nu(\text{C-H})_{\text{ar}}$ 3079; $\nu(\text{C-H})_{\text{imin}}$ 3028; $\nu_{\text{as}}(\text{C-H})$ 2939; $\nu(\text{C=C})_{\text{ar}}$ 1614, 1523; $\nu(\text{C=N})$ 1464; $\delta(\text{CH}_3)$ 1285; $\nu(\text{C-N})$ 1235; $\gamma(\text{C-H})_{\text{ar}}$ 1004, 910, 891, 810, 783, 760; $\nu(\text{C-S})$ 642.

3.3.3. Complex 3 $[\text{Co}^{\text{II}}\text{L}^3(\text{O-NO}_2)_2(\text{CH}_3\text{OH})]$

Ligand L^3 (35.82 mg, 141.99 μM) was dissolved in 10 mL MeOH. After addition of $\text{Co}(\text{NO}_3)_2 \cdot 6\text{H}_2\text{O}$ (41.31 mg, 141.99 μM) the mixture changed color from yellow to orange. Reaction was carried out for 24 hours at room temperature. Complex was isolated as an orange powder by evaporation of the solvent to ca. 1 mL and precipitation with excess of Et_2O . Brownish monocrystals suitable for X-ray analysis were obtained by slow diffusion of *i*-Pr₂O into a solution of the complex 3 in MeOH at 4 °C. Yield: 60.4 % (40.07 mg)*.

ESI-MS(+) *m/z* (%): 373 (100) $[\text{CoL}^3(\text{NO}_3)]^+$; ESI-MS(-) *m/z* (%): 245 (25) $[\text{Co}(\text{NO}_3)_3]^-$. Anal. calcd. for $\text{C}_{14}\text{H}_{12}\text{N}_6\text{O}_6\text{SCo}$ (467.26): C, 38.56; H, 3.45; N, 17.99%; found: C, 40.37; H, 3.25; N, 17.01%. IR (ATR, cm^{-1}): $\nu(\text{C-H})_{\text{ar}}$ 3040; $\nu(\text{C-H})_{\text{imin}}$ 2976; $\nu(\text{C=C})_{\text{ar}}$ 1635, 1620, 1582, 1564; $\nu(\text{C=N})$ 1461, 1411; $\delta(\text{CH}_3)$ 1289; $\nu(\text{C-O})$ 1254, 1151; $\gamma(\text{C-H})_{\text{ar}}$ 1015, 999, 933, 888, 781, 760. *Yield based on powder.

3.4. X-ray Crystallography

Diffraction data were collected by the ω -scan technique using graphite-monochromated $\text{MoK}\alpha$ radiation ($\lambda = 0.71073 \text{ \AA}$), at 100(1) on Rigaku XCalibur four-circle diffractometer with EOS CCD detector. The data were corrected for Lorentz-polarization as well as for absorption effects [49]. Precise unit-cell parameters were determined by a least-squares fit of the reflections of the highest intensity, chosen from the whole experiment. The structures were solved with SHELXT-2013 [50] and refined with the full-matrix least-squares procedure on F^2 by SHELXL-2013 [51]. All non-hydrogen atoms were refined anisotropically, all hydrogen atoms were placed in idealized positions and refined as "riding model" with isotropic displacement parameters set at 1.2 (1.5 for CH_3) times U_{eq} of appropriate carrier atoms.

The data for the complex 1 were also collected and allowed to confirm the structure of the compound, but the quality of the crystals and the twinning of all samples we tried caused relatively low quality of the results; therefore these data are presented only in the Electronic Supplementary Information (Figure S1, Table S1).

Crystallographic data for the structural analysis has been deposited with the Cambridge Crystallographic Data Centre, Nos. CCDC – 1908252 (1), CCDC – 1908253 (2) and 1908254 (3). Copies of this information may be obtained free of charge from: The Director, CCDC, 12 Union Road, Cambridge, CB2 1EZ, UK; e-mail: deposit@ccdc.cam.ac.uk, or www: www.ccdc.cam.ac.uk.

3.5. Cyclic Voltammetry

3.5.1. Reagents and Solutions

All solutions under investigation were kept at room temperature and purged with high-purity argon (purity 99.998%) before measurements. During measurements the stream of argon was maintained over investigated solution. Aqueous solutions were prepared with deionized water purified in a Millipore Milli-Q system (resistivity $\geq 18 \text{ M}\Omega\text{cm}^{-1}$) and the following chemicals (used as received): KCl, $\text{K}_3[\text{Fe}(\text{CN})_6]$, $\text{K}_4[\text{Fe}(\text{CN})_6]$, NaOH, H_2SO_4 , 30% H_2O_2 , acetone from POCh (Gliwice, Poland). TBAP and DMF were from Sigma Aldrich. The solutions of 0.1 M NaOH in water and 0.1 M TBAP in DMF were used in measurements as supporting electrolytes.

3.5.2. Electrodes

The working electrode was the gold electrode (purity 99.999%). As a counter electrode (2 cm^2) a gold sheet was used. Gold was purchased from the Polish State Mint. As a reference electrode the saturated calomel electrode (SCE) from the EuroSensor, Poland was used. Before measurements with studied complexes the working Au electrode was cleaned and activated electrochemically. In the order to clean, the Au surface was polished with aluminum slurries of successively decreasing final grades (down to $0.05 \mu\text{m}$, Buehler) on polishing cloths (Buehler). Then it was rinsed carefully with water purified in a Millipore Milli-Q system (resistivity $\geq 18 \text{ M}\Omega\text{cm}^{-1}$). After cleaning the working electrode was electrochemically activated by cycling its potential with scan rate $dE/dt = 0.1 \text{ V}\cdot\text{s}^{-1}$ in the potential range between where the onset of hydrogen and oxygen evolution appears (in this range no faradic reactions occur on the gold surface) in 0.1 M NaOH solution. For the used electrode it was the following potential range: -1.1 vs. SCE to $E = 0.65 \text{ V vs. SCE}$. This procedure allows avoiding structural changes on the gold surface and remaining the roughness factor of electrode constant [52].

The effective surface area of the working Au electrode was determined electrochemically by carrying out the experiments in which the oxidation/reduction of equimolar amount (0.005 M) of electrochemical probe $[\text{Fe}(\text{CN})_6]^{4-}/[\text{Fe}(\text{CN})_6]^{3-}$ in 0.5 M KCl was tested with different scan rates of applying potential to this electrode (Figure S9). From the electrochemical theory it is well-known that the absolute value of the intensity of current peak i_p [mA] appropriate for reversible redox process in stationary redox systems is described by Randles–Sevcik equation [34]: $i_p = (2.99 \cdot 10^5) n^{3/2} A c D^{1/2} v^{1/2}$ in which $2.99 \cdot 10^5$ is the numerical constant; i_p [mA] is the intensity of a current at the maximum of the oxidation/reduction peak; n is the number of electrons exchanged in a tested electrochemical system; A is the electrode area [cm^2]; c [M] denotes a concentration of electroactive probe inside the supporting electrolyte solution; D [$\text{cm}^2\cdot\text{s}^{-1}$] represents the diffusion coefficient; and v [$\text{V}\cdot\text{s}^{-1}$] is the potential scan rate. From the Randles–Sevcik's equation it is evident that the intensity of current at the potential of respective peak is directly proportional to the square root of scan rate for the tested samples. By using the least squares method and assuming that in the studied system $D = 9 \cdot 10^{-6} \text{ cm}^2\cdot\text{s}^{-1}$ [53] and $n = 1$, from the obtained value of slopes of rectilinear $i_p-v^{1/2}$ dependences, value of the surface area of the used Au electrode was calculated to be $A = 0.07 \text{ cm}^2$.

At the end of each series of experiments in non-aqueous solutions, Au electrodes were rinsed with acetone and water and the working electrode was electroactivated again in the way described above. The shapes of cyclic voltammograms recorded in each series of experiments were the same as those taken before the measurements in non-aqueous solutions. This means that the surface of the working electrode did not alter during the experiment.

3.6. Photocatalytic Studies

3.6.1. Photocatalytic and Degradation Experiments

The stock solutions of the dyes: RB21 and AR18 were prepared by dissolving of 0.2 g of the appropriate substance and dissolving it in 100 mL of MilliQ water. Working solutions of the desired concentration were prepared by diluting the stock solutions with MiliQ water.

Volumes of 50 mL of the working solution of the dye at concentration 50 mg/L and 2 mg of the tested catalyst (TiO₂ or complexes) were transferred to the glass crystallization dishes. Before the irradiation the dye-catalyst suspension was kept in the dark with stirring for 1 h to establish an adsorption-desorption equilibrium.

Next, the equilibrated suspension was exposed to a radiation in the solar simulator for 2 h. In order to determine the dye degradation, 2 mL of sample was collected at regular intervals of 15 min. and centrifuged to remove the photocatalyst and their UV-Vis spectra were recorded. In the case of turbid samples, each measurement was preceded by the centrifugation of 4 mL of the sample. After recording the UV spectrum, the content of the cuvette was transferred again to the reaction dish. It was noted that the volume of the solution did not change (in the simulator chamber the temperature was *ca.* 30°C). If necessary, the content of the crystallizer was supplemented with MiliQ water to the starting volume of 50 mL.

3.6.2. Photostability Experiments

A total of 5 mg samples of the tested compounds 1–3 was weighted into a Petri dish. The weight was spread to create a relatively thin layer. Then it was exposed for 120 min UV radiation ($\lambda = 256$ nm) or in the imaging chamber of a solar light. The IR and PXRD were recorded before and after irradiation.

4. Conclusions

Herein, we aimed to investigate the potential of Co(II/III) complexes as catalysts of organic waste decay that utilize visible light more efficiently than TiO₂. We employed in our study a “closed” complex 1 with coordination sphere filled with two N₂O-donor organic ligands HL¹ and two “open” complexes 2 and 3 coordinated by one ligand (L² and L³, respectively) and by labile inorganic ligands. L² comprises the benzothiazole moiety, while L³ has a quasi-reversibly oxidizing benzoxazole unit.

We have synthesized the cobalt complexes as a continuation of our previous work concerning photocatalytical properties of Ag(I) compounds [28]. The modification of metallic center was dictated by a pursuit to obtain catalyst with even lower HOMO-LUMO gaps and been able to digest visible light more efficiently. In case of Ag(I) complexes the HOMO-LUMO gap was *ca.* 2.73 eV, while here it is 1.77 eV for the most active complex 2 (for TiO₂ the HOMO-LUMO gap is 3.2 eV). So, in fact, incorporating Co(II) ions instead of Ag(I) has improved the parameters of potential photocatalysts. Moreover, the study on photocatalytic activity of presented complexes supported by electrochemical measurements implies that the more electrochemically stable compound, the better photocatalyst it is. In our study the leading compound is “open” complex 2 with N₃-donor ligand comprising benzothiazole unit. Since it has been reported as the efficient catalyst for Acid Red 18 digestion, which is an azo-dye, our future task is to assess its ability to decompose other azo-dyes, such as Reactive Red 198 and Reactive Black 5 and optimize the experimental conditions to streamline the process.

Supplementary Materials: Supplementary materials can be found at <http://www.mdpi.com/2073-4344/9/11/913/s1>. Table S1. Crystal data, data collection and structure refinement for complexes 1, 2 and 3; Table S2. Relevant geometrical parameters (Å, °) with standard uncertainties in parentheses. A, B and C are the least-squares planes of 6+5 system, C-N-N=C=C linker and phenyl/pyridine ring, respectively; Figure S1. Perspective view of the complex 1; ellipsoids are drawn at the 50% probability level, hydrogen atoms are represented by spheres of arbitrary radii; Figure S2. Cyclic voltammograms of the polycrystalline gold electrode in basic electrolyte 0.1 M TBAP in DMF. dE/dt = 0.1 V s⁻¹; Figure S3. Cyclic voltammograms of the polycrystalline gold electrode in basic electrolyte 0.1 M TBAP in DMF and increasing amounts (10⁻⁵ M ÷ 10⁻³ M) of complex 1. dE/dt = 0.1 V s⁻¹. Figure S3. Cyclic voltammograms of the polycrystalline gold electrode in basic electrolyte 0.1 M TBAP in DMF

and increasing amounts (10^{-5} M \div 10^{-3} M) of complex **1**. $dE/dt = 0.1$ V s^{-1} . Figure S5. Cyclic voltammograms of the polycrystalline gold electrode in basic electrolyte 0.1 M TBAP and increasing amounts (10^{-5} M \div 10^{-3} M) of complex **3**. $dE/dt = 0.1$ V s^{-1} . Figure S6. Cyclic voltammograms of the polycrystalline gold electrode in basic electrolyte 0.1 M TBAP in DMF and comparison of complex **1** and parent ligand HL¹. $dE/dt = 0.1$ V s^{-1} . Figure S7. Cyclic voltammograms of the polycrystalline gold electrode in basic electrolyte 0.1 M TBAP in DMF and comparison of complex **2** and parent ligand L². $dE/dt = 0.1$ V s^{-1} . Figure S8. Cyclic voltammograms of the polycrystalline gold electrode in basic electrolyte 0.1 M TBAP in DMF and comparison of complex **3** and parent ligand L³. $dE/dt = 0.1$ V s^{-1} . Figure S9. Cyclic voltammograms recorded at the bare polycrystalline gold electrode in 0.5 M KCl supporting electrolyte solution with $5 \cdot 10^{-3}$ M of $[Fe(CN)_6]^{4-}/[Fe(CN)_6]^{3-}$ recorded at different potential scan rates. Figure S10. The FTIR spectra of complex **1** before (green line) after 120 min irradiation with UV radiation, $\lambda = 256$ nm, (blue line) or in the imaging chamber of a solar light simulator emitting light in the 300–800 nm range (red line). Figure S11. Observed PXRD patterns of complex **1** before (red line) and after irradiation with UV, $\lambda = 256$ nm, (blue line) or in the imaging chamber of a solar light simulator (black line). Figure S12. The FT-IR spectra of complex **2** before (green line) and after 120 min. of irradiation with UV radiation, $\lambda = 256$ nm, (blue line) or in the imaging chamber of a solar light simulator emitting light in the 300–800 nm range (red line). The irradiation showed small differences in the spectra spectrum changes in the complex **2**. A slight band change is observed at wavenumber 1464 cm^{-1} , 1468 cm^{-1} VIS, 1466 cm^{-1} UV. This band is responsible for CH₂ deformation bonds. Figure S13. Observed PXRD patterns of the complex **2** before (red line) and after irradiation with UV, $\lambda = 256$ nm, (blue line) or in the imaging chamber of a solar light simulator (black line). Figure S14. The FT-IR spectra of complex **3** before (green line) and after 120 min. of irradiation with UV radiation, $\lambda = 256$ nm, (blue line) or in the imaging chamber of a solar light simulator emitting light in the 300–800 nm range (red line). Figure S15. Observed PXRD patterns of the complex **3** before (red line) and after irradiation with UV, $\lambda = 256$ nm, (blue line) or in the imaging chamber of a solar light simulator (black line). Figure S16. Absorption spectrum of Reactive Blue 21 at 50 mg/L concentration. Figure S17. Absorption spectrum of Acid Red 18 at 50 mg/L concentration.

Author Contributions: M.S.: repeated syntheses and full characterization of ligands HL¹, L² and L³, synthesis and full characterization of complexes **1–3**, writing—original draft preparation; W.C.: first synthesis and full characterization of ligand HL¹; C.H.: photocatalytic, photostability, and optical measurements; R.Ś.: optical measurements and their description; T.Ł.: cyclic voltammetry measurements and their description; M.K.: X-ray measurements and description of crystal structures; J.K.: photocatalytic, photostability, optical measurements and their description; M.A.F.-J.: conceptualization, first synthesis of ligand L²–L³, writing—final version of manuscript, review and editing; V.P.: supervision, writing—review and editing.

Funding: M.A.F.-J.: The work was supported by the National Science Centre in Poland in the framework of Sonatina grant no. 2017/24/C/ST5/00181. M.S. and W.C.: This work was supported by the grant no. POWR.03.02.00-00-I026/16 co-financed by the European Union through the European Social Fund under the Operational Program Knowledge Education Development. The NanoPlus apparatus, UV/Vis/NIR and UV/Vis spectrophotometers, and Agilent Technologies Super Nova X-ray diffractometer were funded by the EU, as part of the Operational Programme Development of Eastern Poland, projects POPW.01.03.00-20-034/09-00 and POPW.01.03.00-20-004/11-00.

Conflicts of Interest: The authors declare no conflict of interest.

Abbreviations

AR18	Acid Red 18
CV	cyclic voltammetry
DMF	dimethylformamide
DR	diffuse-reflectance
RB21	Reactive Blue 21
SCE	saturated calomel electrode
TBAP	tetrabutylammonium perchlorate

References

- Han, X.; Han, Z.; Li, J.; Zhao, J.; Zhao, X. Coordinative integration of copper (II) and iron (II) phthalocyanine into amidoximated PAN fiber for enhanced photocatalytic activity under visible light irradiation. *J. Colloid Interface Sci.* **2019**, *533*, 333–343. [[CrossRef](#)]
- Ghoreishi, S.M.; Haghghi, R. Chemical catalytic reaction and biological oxidation for treatment of non-biodegradable textile effluent. *Chem. Eng. J.* **2003**, *95*, 163–169. [[CrossRef](#)]
- Zollinger, H. *Color Chemistry. Synthesis, Properties and Applications of Organic Dyes and Pigments*; VCH Publishers: New York, NY, USA, 1987; pp. 92–100.

4. Silva, M.C.; Corrêa, A.D.; Amorim, M.T.S.P.; Parpot, P.; Torres, J.A.; Chagas, P.M.B. Decolorization of the phthalocyanine dye reactive blue 21 by turnip peroxidase and assessment of its oxidation products. *J. Mol. Catal. B Enzym.* **2012**, *77*, 9–14. [[CrossRef](#)]
5. Zhang, L.; Zhao, Y.; Zhong, L.; Wang, Y.; Chai, S.; Yang, T.; Han, X. Cu₂S-Cu-TiO₂ mesoporous carbon composites for the degradation of high concentration of methyl orange under visible light. *Appl. Surf. Sci.* **2017**, *422*, 1093–1101. [[CrossRef](#)]
6. Matthews, R.D.; Bottomley, L.A.; Pavlostathis, S.G. Palladium-catalyzed hydrogen reduction and decolorization of reactive phthalocyanine dyes. *Desalination* **2009**, *248*, 816–825. [[CrossRef](#)]
7. Alves de Lima, R.O.; Bazo, A.P.; Salvadori, D.M.F.; Rech, C.M.; de Palma Oliveira, D.; de Aragão Umbuzeiro, G. Mutagenic and carcinogenic potential of a textile azo dye processing plant effluent that impacts a drinking water source. *Mutat. Res. Genet. Toxicol. Environ. Mutagen.* **2007**, *626*, 53–60. [[CrossRef](#)] [[PubMed](#)]
8. Brüscheweiler, B.J.; Merlot, C. Azo dyes in clothing textiles can be cleaved into a series of mutagenic aromatic amines which are not regulated yet. *Regul. Toxicol. Pharmacol.* **2017**, *88*, 214–226. [[CrossRef](#)] [[PubMed](#)]
9. Katheresan, V.; Kannedo, J.; Lau, S.Y. Efficiency of various recent wastewater dye removal methods: A review. *J. Environ. Chem. Eng.* **2018**, *6*, 4676–4697. [[CrossRef](#)]
10. Xia, S.-J.; Liu, F.-X.; Ni, Z.-M.; Shi, W.; Xue, J.-L.; Qian, P.-P. Ti-based layered double hydroxides: Efficient photocatalysts for azo dyes degradation under visible light. *Appl. Catal. B* **2014**, *144*, 570–579. [[CrossRef](#)]
11. Chen, Z.; Xu, Y.-J. Ultrathin TiO₂ layer coated-CdS spheres core-shell nanocomposite with enhanced visible-light photoactivity. *ACS Appl. Mater. Interfaces* **2013**, *5*, 13353–13363. [[CrossRef](#)] [[PubMed](#)]
12. Deng, Y.; Chen, Y.; Chen, B.; Ma, J. Preparation, characterization and photocatalytic activity of CuBi₂O₄/NaTaO₃ coupled photocatalysts. *J. Alloys Compd.* **2013**, *559*, 116–122. [[CrossRef](#)]
13. Di Paola, A.; García-López, E.; Marci, G.; Palmisano, L. A survey of photocatalytic materials for environmental remediation. *J. Hazard. Mater.* **2012**, *211–212*, 3–29. [[CrossRef](#)] [[PubMed](#)]
14. Wang, Y.; Zhang, R.; Li, J.; Li, L.; Lin, S. First-principles study on transition metal-doped anatase TiO₂. *Nanoscale Res. Lett.* **2014**, *9*, 46. [[CrossRef](#)] [[PubMed](#)]
15. Dostani, M.; Kianfar, A.H.; Momeni, M.M. Visible light photocatalytic activity of novel Ni²⁺, Cu²⁺ and VO₂ complexes derived from vanillin bidentate Schiff base ligand doped on TiO₂ nanoparticles. *J. Mater. Sci. Mater. Electron.* **2017**, *28*, 633–640. [[CrossRef](#)]
16. Eshwar Rao, S.; Gayathri, V. Poly(styrene-divinyl benzene)-immobilized Fe(III) complex of 1,3-bis(benzimidazolyl)benzene: Efficient catalyst for the photocatalytic degradation of xylenol orange. *J. Appl. Polym. Sci.* **2018**, *135*, 46480. [[CrossRef](#)]
17. Qin, L.; Hu, Q.; Wu, Y.; Cai, J.-L.; Li, Y.-Y. Three novel Co(ii)/Ni(ii)-based coordination polymers as efficient heterogeneous catalysts for dye degradation. *CrystEngComm* **2018**, *20*, 4042–4048. [[CrossRef](#)]
18. Qiao, Y.; Ren, S.-S.; Liu, L.-H.; Guan, W.-S.; Li, Z.-M.; Che, G.-B.; Liu, C.-B.; Wang, Y.-Y.; Wang, Q.-W.; Li, X.-Y.; et al. Adsorption and photocatalytic properties of transition metal Zinc(II) complex based on 5-(4-(tetrazol-5-yl)phenyl)isophthalic acid. *J. Mol. Struct.* **2018**, *1161*, 238–245. [[CrossRef](#)]
19. Xu, Z.; Li, Q.; He, X.; Li, H.; Wang, Y.; Cao, J. Construction of mixed-valence Cu(I)/Cu(II) 3-D framework and its photocatalytic activities. *Polyhedron* **2018**, *151*, 478–482. [[CrossRef](#)]
20. Malato, S.; Blanco, J.; Vidal, A.; Richter, C. Photocatalysis with solar energy at a pilot-plant scale: An overview. *Appl. Catal. B* **2002**, *37*, 1–15. [[CrossRef](#)]
21. Casero, I.; Sicilia, D.; Rubio, S.; Pérez-Bendito, D. Chemical degradation of aromatic amines by Fenton's reagent. *Water Res.* **1997**, *31*, 1985–1995. [[CrossRef](#)]
22. Perkowski, J.; Jóźwiak, W.; Kos, L.; Stajszczyk, P. Application of fenton's reagent in detergent separation in highly concentrated water solutions. *Fibres Text. East. Eur.* **2006**, *14*, 114–119.
23. Barbusiński, K. The modified fenton process for decolorization of dye wastewater. *Polish J. Environ. Stud.* **2005**, *14*, 281–285.
24. Li, X.; Xiong, Z.; Ruan, X.; Xia, D.; Zeng, Q.; Xu, A. Kinetics and mechanism of organic pollutants degradation with cobalt-bicarbonate-hydrogen peroxide system: Investigation of the role of substrates. *Appl. Catal. A* **2012**, *411–412*, 24–30. [[CrossRef](#)]
25. Xu, A.; Li, X.; Ye, S.; Yin, G.; Zeng, Q. Catalyzed oxidative degradation of methylene blue by in situ generated cobalt (II)-bicarbonate complexes with hydrogen peroxide. *Appl. Catal. B* **2011**, *102*, 37–43. [[CrossRef](#)]
26. Spier, E.; Neuenschwander, U.; Hermans, I. Insights into the Cobalt(II)-Catalyzed Decomposition of Peroxide. *Angew. Chem. Int. Ed.* **2013**, *52*, 1581–1585. [[CrossRef](#)] [[PubMed](#)]

27. Song, Q.; Jia, M.; Ma, W.; Fang, Y.; Huang, Y. Heterogeneous degradation of toxic organic pollutants by hydrophobic copper Schiff-base complex under visible irradiation. *Sci. China Chem.* **2013**, *56*, 1775–1782. [[CrossRef](#)]
28. Fik, M.A.; Kubicki, M.; Odachowska, A.E.; Karpińska, J.; Patroniak, V. Helicity in photocatalysis—advantage or obstacle? Studies on silver complexes—synthesis, structure, and photocatalytic Activity. *Eur. J. Inorg. Chem.* **2016**, *2016*, 5530–5538. [[CrossRef](#)]
29. Fik, M.A.; Czepa, W.; Kubicki, M.; Patroniak, V. Formation of non-covalent porous framework with Fe ions and N2O Schiff base ligand: Structural and thermal studies. *Supramol. Chem.* **2017**, *29*, 643–650. [[CrossRef](#)]
30. Fik, M.A.; Löffler, M.; Weselski, M.; Kubicki, M.; Korabik, M.J.; Patroniak, V. New Fe(II) complexes with Schiff base ligand: Synthesis, spectral characterization, magnetic studies and thermal stability. *Polyhedron* **2015**, *102*, 609–614. [[CrossRef](#)]
31. Gorczyński, A.; Pakulski, D.; Szymańska, M.; Kubicki, M.; Bułat, K.; Łuczak, T.; Patroniak, V. Electrochemical deposition of the new manganese(II) Schiff-base complex on a gold template and its application for dopamine sensing in the presence of interfering biogenic compounds. *Talanta* **2016**, *149*, 347–355. [[CrossRef](#)]
32. Newman, R.C.; Burstein, G.T. Reactions of scratched gold electrodes in alkaline solution. *J. Electroanal. Chem.* **1981**, *129*, 343–348. [[CrossRef](#)]
33. Marcinkowski, D.; Fik, M.A.; Łuczak, T.; Kubicki, M.; Patroniak, V. New Mn(II) complexes with benzoxazole-based ligands: Synthesis, structure and their electrochemical behavior. *Polyhedron* **2018**, *141*, 125–132. [[CrossRef](#)]
34. Bard, A.J.; Faulkner, L.R. *Electrochemical Methods: Fundamentals and Applications*; Wiley: New York, NY, USA, 2001.
35. Garrell, R.L.; Chadwick, J.E.; Severance, D.L.; McDonald, N.A.; Myles, D.C. Adsorption of sulfur containing molecules on gold: The effect of oxidation on monolayer formation and stability characterized by experiments and theory. *J. Am. Chem. Soc.* **1995**, *117*, 11563–11571. [[CrossRef](#)]
36. Xu, S.; Podoprygorina, G.; Böhmer, V.; Ding, Z.; Rooney, P.; Rangan, C.; Mittler, S. Tetraurea calix[4]arenes with sulfur functions: Synthesis, dimerization to capsules, and self-assembly on gold. *Org. Biomol. Chem.* **2007**, *5*, 558–568. [[CrossRef](#)]
37. Savarino, P.; Viscardi, G.; Quagliotto, P.; Perracino, P.; Barni, E. Voltammetric behaviour of heterocyclic systems. Pyridyl-substituted benzimidazoles, benzoxazoles and benzothiazoles. *J. Heterocyclic Chem.* **1997**, *34*, 1479–1485. [[CrossRef](#)]
38. Komissarov, A.N.; Makarov, D.A.; Yuzhakova, O.A.; Savvina, L.P.; Kuznetsova, N.A.; Kaliya, O.L.; Lukyanets, E.A.; Negrimovsky, V.M. Synthesis and some properties of phosphonomethyl substituted phthalocyanines. *Macroheterocycles* **2012**, *5*, 169–174. [[CrossRef](#)]
39. Khataee, A.R.; Kasiri, M.B. Photocatalytic degradation of organic dyes in the presence of nanostructured titanium dioxide: Influence of the chemical structure of dyes. *J. Mol. Catal. A Chem.* **2010**, *328*, 8–26. [[CrossRef](#)]
40. Iasco, O.; Novitchi, G.; Jeanneau, E.; Tommasino, J.B.; Roques, N.; Luneau, D. Versatile chemical transformations of benzoxazole based ligands on complexation with 3d-metal ions. *Inorg. Chem.* **2012**, *51*, 2588–2596. [[CrossRef](#)]
41. Ananthakrishnan, S.J.; Kumar, B.S.; Somanathan, N.; Mandal, A.B. Supramolecular assembly in side-chain conjugated thiophene copolymers. *RSC Adv.* **2013**, *3*, 8331–8340. [[CrossRef](#)]
42. Qu, Y.; Duan, X. Progress, challenge and perspective of heterogeneous photocatalysts. *Chem. Soc. Rev.* **2013**, *42*, 2568–2580. [[CrossRef](#)]
43. Almeida Guerra, W.N.; Teixeira Santos, J.M.; Raddi de Araujo, L.R. Decolorization and mineralization of reactive dyes by a photocatalytic process using ZnO and UV radiation. *Water Sci. Technol.* **2012**, *66*, 158–164. [[CrossRef](#)] [[PubMed](#)]
44. Miklos, D.B.; Remy, C.; Jekel, M.; Linden, K.G.; Drewes, J.E.; Hübner, U. Evaluation of advanced oxidation processes for water and wastewater treatment—A critical review. *Water Res.* **2018**, *139*, 118–131. [[CrossRef](#)] [[PubMed](#)]
45. Srivastava, P.; Goyal, S.; Patnala, P.K. Degradation of reactive, acid and basic textile dyes in the presence of ultrasound and rare earths [Lanthanum and Praseodymium]. *Ultrason. Sonochem.* **2014**, *21*, 1994–2009. [[CrossRef](#)] [[PubMed](#)]

46. Olya, M.E.; Pirkarami, A. On the positive role of doping Cu and N2 on TiO2 in improving dye degradation efficiency: Providing reaction mechanisms. *Korean J. Chem. Eng.* **2015**, *32*, 1586–1597. [[CrossRef](#)]
47. Wałęsa-Chorab, M.; Patroniak, V.; Kubicki, M.; Kądziołka, G.; Przepiórski, J.; Michalkiewicz, B. Synthesis, structure, and photocatalytic properties of new dinuclear helical complex of silver(I) ions. *J. Catal.* **2012**, *291*, 1–8. [[CrossRef](#)]
48. Marcinkowski, D.; Wałęsa-Chorab, M.; Patroniak, V.; Kubicki, M.; Kądziołka, G.; Michalkiewicz, B. A new polymeric complex of silver(i) with a hybrid pyrazine–bipyridine ligand—synthesis, crystal structure and its photocatalytic activity. *New J. Chem.* **2014**, *38*, 604–610. [[CrossRef](#)]
49. Rigaku Oxford Diffraction. *CrysAlis PRO (Version 1.171.38.41)*; Rigaku Oxford Diffraction: Yarnton, UK, 2015.
50. Sheldrick, G.M. SHELXT—Integrated space-group and crystal-structure determination. *Acta Cryst. A* **2015**, *71*, 3–8. [[CrossRef](#)]
51. Sheldrick, G.M. Crystal structure refinement with SHELXL. *Acta Cryst. C* **2015**, *71*, 3–8. [[CrossRef](#)]
52. Łuczak, T. Adsorption of methylamine at a polycrystalline gold/solution interface. *Coll. Surf. A* **2006**, *280*, 125–129. [[CrossRef](#)]
53. Available online: www.reaxys.com (accessed on 2 October 2019).



© 2019 by the authors. Licensee MDPI, Basel, Switzerland. This article is an open access article distributed under the terms and conditions of the Creative Commons Attribution (CC BY) license (<http://creativecommons.org/licenses/by/4.0/>).